Meso scale flextensional piezoelectric actuators

IOP Publishing Smart Materials and Structures
Smart Mater. Struct. **27** (2018) 015008 (10pp) https://doi.org/10.1088/1361-665X/aa9366

Meso scale flextensional piezoelectric actuators

Peter A York[1,2], **Noah T Jafferis**[1,2] **and Robert J Wood**[1,2]

[1] John A Paulson School of Engineering and Applied Sciences, Harvard University, Cambridge, MA, USA
[2] Wyss Institute for Biologically Inspired Engineering, Harvard University, Boston, MA, USA

E-mail: pyork@g.harvard.edu

Received 24 August 2017, revised 11 October 2017
Accepted for publication 13 October 2017
Published 27 November 2017

Abstract

We present an ultra-thin meso scale piezoelectric actuator consisting of a piezoceramic beam and a carbon fiber displacement-amplification frame. We show that the actuator can be designed to achieve a wide range of force/displacement characteristics on the mN/μm scales. The best performing design achieved a free displacement of 106 μm and a blocked force of 73 mN, yielding a total energy density of 0.51 Jkg^{-1} for the 7.6 mg system. We describe a printed circuit MEMS process for fabricating the actuator that incorporates laser micromachining, chemical vapor deposition, and precision carbon fiber lamination. Lastly, we report the incorporation of the actuator into a microgripper and describe other promising application opportunities in micro-optics and micro-laser systems.

Keywords: piezoelectric actuators, meso scale devices, multi-material laminates, laser micromachining, micromanipulation

(Some figures may appear in colour only in the online journal)

1. Introduction

Piezoelectric actuators are an attractive option for producing accurate, high-force, high-bandwidth motion due to their high intrinsic stiffness and force density. They are particularly attractive for meso scale devices such as micro-air vehicles, surgical tools, and optics assemblies due to their favorable scaling physics: for planar devices with constant thickness, force and displacement scale with the characteristic length L, and natural frequency scales with L^{-1}. We define the 'meso' scale to be the set of lengths between one and ten millimeters; thus, it resides in between the 'micro' scale, which consists of lengths less than millimeter (e.g. MEMS devices), and the 'macro' scale, which contains lengths greater than ten millimeters. However, there are two key challenges to overcome in creating piezoelectric actuators for use in meso scale systems: (1) amplifying the low intrinsic displacements produced by piezoceramics (typically several μm) and (2) manufacturing and assembling actuators on a scale much smaller than macro scale nuts-and-bolts approaches but not as small as that of typical MEMS techniques. Researchers have addressed the former challenge on the micro and macro scales through a variety of techniques, but the latter challenge remains largely unexplored. Here we apply the lessons learned on the micro and macro scales towards the design and fabrication of meso scale displacement-amplified piezoelectric actuators.

Different techniques exist for amplifying piezo displacements, and each has merits and demerits. The most common technique is internal leveraging, in which longitudinal strain is converted to bending through the addition of passive layers of material that shift the neutral bending plane. Such actuators include bimporhs and unimorphs on the macro [1–3], meso [4], and micro scales [5]. On the micro scale, internal leveraging has also been used to create pseudo in-plane motion with cascaded antagonistic unimorphs [6]. A key advantage of these devices is that they typically require little passive material to achieve amplification, which serves to increase energy density. Moreover, the lack of additional serial compliance in transmission elements generally serves to increase output impedance. However, the material is not strained uniformly through its thickness during bending, which is a material inefficiency and can lead to short lifetimes, due to elevated stress on the outer surfaces. Furthermore, the tip of a bending actuator traces out an arc that only approximates linear motion, which is a limitation in some applications.

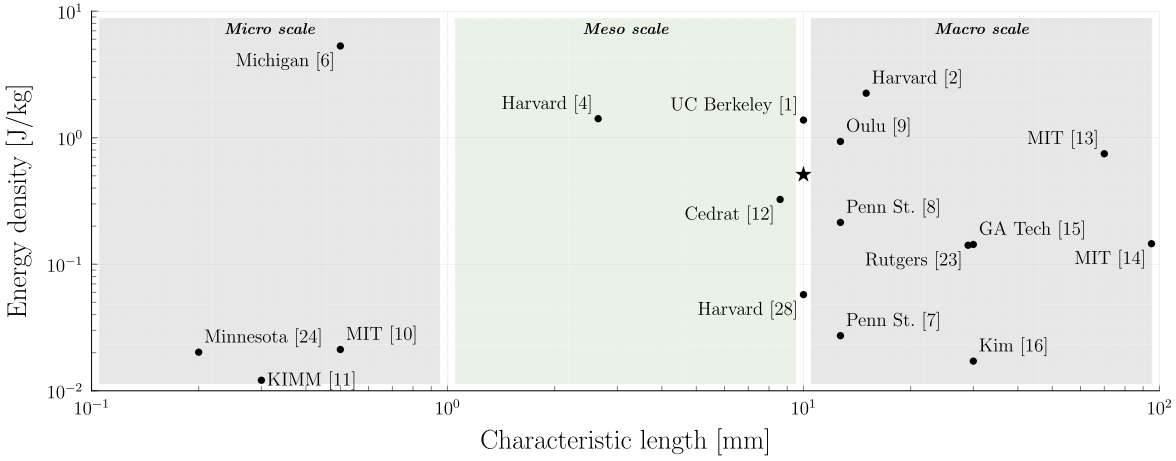

Figure 1. State-of-the-art displacement-amplified piezoelectric actuators on the micro, meso, and macro scale, respectively. Mechanical energy density (calculated as $1/2F_{\text{block one-way}}\Delta x_{\text{free}}m^{-1}$) is plotted versus characteristic length. We see that most existing solutions are clustered near the extremes of scale. The best performing actuator described herein is marked ★.

The second most common technique for amplifying piezoceramic displacements is external leveraging, in which additional passive elements are added in a transmission to trade off force for displacement. These have been predominately produced on the macro scale [7–9] but have also been explored on the micro scale [10, 11] and to a limited extent on the meso scale [12]. Variations on this approach include using buckling [13, 14] or nesting [15, 16] to further amplify motion. With the exception of [10], each of these designs has used piezoceramic stacks as their active elements. Advantages include truly linear motion and uniform straining of the active material, which should result in higher efficiency and longer lifetimes. A key disadvantage is that the addition of passive elements to an actuator inherently reduces its energy density. More subtly, it is challenging to not introduce unwanted serial or parallel compliances while introducing passive elements.

A third common technique for amplifying displacements is frequency leveraging. Actuators that use this principle typically have a vibrating stator that incrementally moves a rotor. Due to this construction, these devices are typically termed 'motors'. Overviews of these devices can be found in [17–19]. On the macro scale, these devices typically use a ratcheting and locking principle [20], but on the meso and micro scale, stick-slip (i.e., inchworm) drives [21] or friction couplings driven by standing or traveling waves [22] are more common.

Lastly, one can amplify piezoelectric displacements using clever tricks with device geometry. A prime example is a macro scale spiral actuator [23] fabricated through fused ceramic deposition (nozzle deposited and sintered) and radially polarized, such that a large effective actuator length is packed inside a small area. The transverse displacements produced are thus much larger than if the actuator was a simple beam within the same area. A similar device [24] uses a meander-line geometry to increase the effective actuation length for a given area.

The primary reason for the current dearth of piezoelectric actuators on the meso scale is the dual challenge of manufacturing and assembly. On the micro scale, well-developed MEMs techniques (i.e., metal-organic chemical vapor deposition and sol-gel deposition [25]) can be used. An overview of the development of processing techniques for thin-film PZT deposition and integration can be found in [26]. Similarly, on the macro scale, standard manufacturing processes such as milling, molding, 3D-printing, and machine assembly can be used. Challenges arise, however, on the meso scale, on which the most suitable manufacturing techniques are laser micromachining, micro wire electron discharge machining, and micro powder blasting, all of which are subtractive techniques; the difficulty of manufacturing on the meso scale is due in part to the lack of viable additive techniques. Related to this is the larger challenge of accurately assembling constituent parts on the meso scale.

We overcame these challenges by utilizing a meso scale manufacturing paradigm known as printed circuit MEMS (PC-MEMS), so called because it incorporates printed circuit fabrication techniques with traditional MEMS processes [27]. Core to this technique is the use of laser micromachining to create complex 2D geometries and the use of pin-aligned heat/weight presses to precisely align and bond layers of different materials. Minimum feature size is governed by the accuracy, repeatability, and spot size of the laser micromachining system, and typically is $\sim$20 μm. Maximum in-plane feature size is limited by the field of view of the system but is typically acceptable for small-batch meso scale device manufacturing.

Using PC-MEMS, we were able to create a meso scale flextensional actuator that increases by a factor of 20 the low intrinsic piezoelectric displacement via geometric amplification. Our meso scale device is similar to the micro scale device in [10] and uses materials and manufacturing techniques similar to the macro scale device in [2]. It amplifies the d_{31} contraction of the piezoceramic PZT-5H through a four-bar linkage fabricated from high-modulus carbon fiber. Other materials used include copper, polyimide, and parylene.

Through careful material selection and design optimization, we achieved an energy density that exceeds that of most existing devices (figure 1). We began by deriving lumped parameter and finite element models, described in

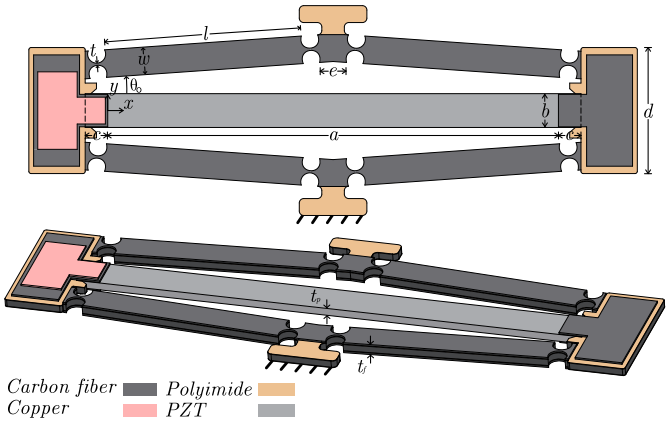

	Description	Typical Value
a	piezo length	8 [mm]
b	piezo width	1 [mm]
c	bridge length	0.4 [mm]
d	frame height	2 [mm]
e	output link width	0.6 [mm]
l	linkage arm length	3.5 [mm]
θ_0	nominal linkage angle	4 [deg]
t	flexure thickness (in-plane)	20 [μm]
t_f	frame thickness (out-of-plane)	195 [μm]
t_p	piezo thickness (out-of-plane)	135 [μm]
w	linkage arm width	490 [μm]

Figure 2. Flextensional actuator design schematic with materials and geometric parameters. Descriptions and typical values are shown on right.

sections 2 and 3, respectively. We then conducted a model sensitivity analysis, from which we performed a design study on the most critical parameters, as reported in section 4. We fabricated the generated actuator designs and measured their blocked force and free displacement voltage responses using the measurement techniques described in section 5. Transient step response, repeatability, and resolution are also shown. We found that a wide range of output force/displacement characteristics can be achieved and that the models well predict the trends in the experimental results. Manufacturing and assembly are essential components of this work and are described in detail in section 6. Lastly, with a view toward applications, we incorporated an actuator into a microgripper and fabricated down-scaled versions, which are shown in section 7.

2. Lumped parameter model

We began the design process by simplifying the schematic shown in figure 2 to the lumped parameter model shown in figure 3. The piezoelectric element is replaced by a force source of magnitude f in parallel with a spring of stiffness k_p. The compressive force f is given by:

$$f = f_{31} Vb \tag{1}$$

where f_{31} is an intrinsic material parameter that relates the stress generated in the piezoceramic to the applied electric field. Note that f_{31} depends both on the applied electric field as well as the current strain state, and we use the empirical model from [2]. The stiffness k_p is equal to the compressive stiffness of the piezoelectric element, which is a function of the elastic modulus and geometric parameters. Note that the elastic modulus of PZT-5H increases with increasing compressive strain, and we use the empirical model found in [2].

Similarly, the linkage arms are represented by torsional spring elements with stiffness k_t and prismatic springs of stiffness k_c. For simplicity of manufacturing, we restricted ourselves to using circular flexures, for which the torsional and compressive stiffnesses depend on Young's modulus Y_{cf}, flexure thickness t, fillet radius ρ, and frame thickness t_f. For constant fillet radius $\rho = 162.5$ μm, constant frame thickness $t_f = 135$ μm (note that this is an effective thickness that ignores the effect of the low modulus materials, i.e. polyimide, parylene, resin), and constant modulus $Y_{cf} = 100$ GPa, we conducted a simple finite element analysis to determine the flexure stiffnesses as a function of flexure thickness to be:

$$k_t = 0.3878t^2 - 2.00801t + 6.2[\text{N } \mu\text{m}] \tag{2}$$

$$k_{c,f} = -0.0001t^2 + 0.0296t + 0.5233 \text{ [N } \mu\text{m}^{-1}] \tag{3}$$

The magnitude of k_c is given by the series combination of the compressive stiffnesses of the flexure hinges, the linkage arms (treated as simple beams in compression), and the equivalent compressive stiffness due to shear of the member that connects the piezoceramic element to the linkage arm. This latter stiffness was found to be 1 N μm^{-1} via finite element analysis. Lastly, we include a load spring with stiffness k_L in order to capture the actuator response to different loading conditions.

Due to symmetry, only two parameters are needed to represent any configuration; to simplify the analysis, we chose l and θ. To further simplify the analysis, we assumed that links *AI*, *BC*, *DE*, and *GH* have zero length. Then, the static equilibrium equations for the actuator become:

$$\Sigma F_{x,D} = f + 2k_p\Delta x + 2k_c\Delta l c_\theta = 0 \tag{4}$$

$$\Sigma M_{CD,D} = (k_L\Delta y + k_c\Delta l s_\theta)c_\theta + 2k_t\Delta\theta = 0 \tag{5}$$

where $\Delta l = l - l_0$ and $\Delta\theta = \theta - \theta_0$ describe the change from the initial configuration. The output displacement and force are then given by:

$$\Delta y = 2(ls_\theta - l_0 s_{\theta_0}) \tag{6}$$

$$f_{out} = k_L\Delta y \tag{7}$$

Moreover, the displacement amplification achieved by the linkage under no external load ($k_L = 0$) is simply:

$$\lambda = \left|\frac{\Delta y}{2\Delta x}\right| = \left|\frac{ls_\theta - l_0 s_{\theta_0}}{lc_\theta - l_0 c_{\theta_0}}\right| \approx \cot(\theta_0) \tag{8}$$

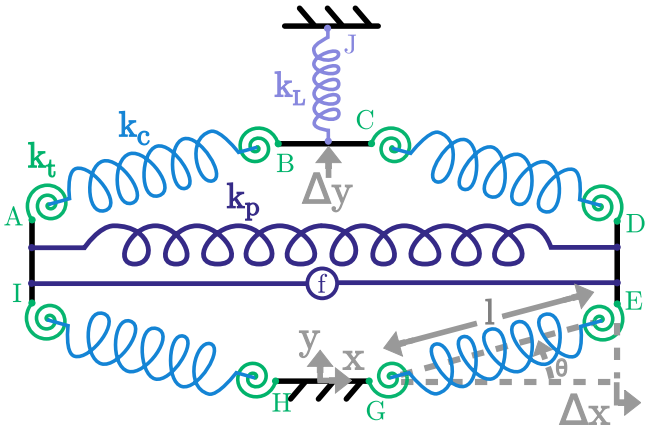

Figure 3. Lumped parameter model of the flextensional actuator. The piezoelectric element becomes a force source in parallel with a prismatic spring, while the flexures and linkage arms become torsional and prismatic springs, respectively. The principle of operation is that a small displacement Δx will produce a much larger displacement Δy due to the geometry of the linkage. Note than $\Delta x < 0$ in normal operation.

where the approximation holds for small Δl and $\Delta\theta$ (i.e. $\Delta l \ll l_0$ and $\Delta\theta \ll \theta_0$). Moreover, in the ideal case, in which the flexures have zero torsional stiffness and the compressive stiffness of the linkage arms is much greater than that of the piezoceramic element, the ratio of the output force to the force generated by the piezoceramic is simply:

$$f_{out}/f = \tan(\theta_0) \tag{9}$$

Because the product of (8) and (9) is unity, we note that the ideal flextensional actuator would be able to do the same work as the piezoceramic element acting alone, albeit with increased displacement and decreased force. The only losses in energy density would be due to the mass of the linkage frame.

3. Finite element model

To validate the lumped parameter model, we created a finite element model to capture the entire device physics and solve the coupled piezoelectricity/solid mechanics problem. All materials were assumed to be homogeneous and elastic. The elastic modulus of the piezoceramic was allowed to vary as a function of strain, and the carbon fiber was treated as orthotropic with the alignment of the fibers along the length of the actuator. Moreover, the piezoelectric coupling coefficient d_{31} was allowed to vary with strain and electric field according to:

$$d_{31} = \frac{f_{31}(\epsilon, E)}{Y(\epsilon)} \tag{10}$$

where E is the applied electric field, and ϵ is the strain in the x-direction. Thus, the strain-charge form of the piezoelectric constitutive relations takes the nonlinear form:

$$\epsilon_{ij} = s_{ijkl}(\epsilon)\sigma_{kl} + d_{kij}(\epsilon, E)E_k \tag{11}$$

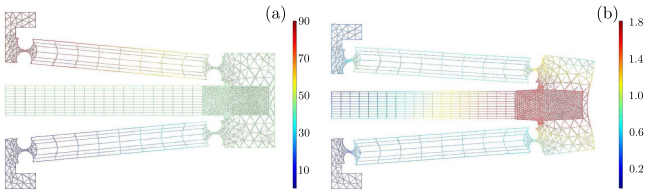

Figure 4. Finite element model of the flextensional actuator using COMSOL Multiphysics 5.2. Free displacement (a) and quasi-blocked force (b) simulations are shown. In both plots, total displacement is shown in μm for a 200 V_{pp} input waveform, and deformation is scaled to facilitate visualization of the results. By exploiting symmetry we both minimize computation time and promote convergence.

$$D_i = d_{ijk}(\epsilon, E)\sigma_{jk} + \varepsilon_{ij}E_j \tag{12}$$

To promote convergence of the nonlinear problem, two simplifying assumptions were made. First, we treated the piezoceramic under the carbon fiber bridges as nonactive material with constant elastic modulus. This is reasonable because the bridge length (denoted c in figure 2) is typically $<10\%$ of the total length of the piezoelectric element and is restricted from contributing to the active deformation by the carbon fiber bridge. Second, we modified the nonlinear stiffness model from [2] in order to slightly smooth the problem; we used $\alpha = 6000$ instead of $\alpha = 8000$ as the value that governs the rate of transition from the low stiffness to high stiffness states. This resulted in only minor changes to the modulus of the piezoceramic ($<4\%$ over strains in the region of interest) and makes the problem much more tractable to solve. Typical results are shown in figure 4.

4. Design

We found reasonable agreement between our finite element and lumped parameter models (see figure 6) and thus felt confident using the lumped parameter model to draw general conclusions about the design space. An increase in the nominal linkage angle θ_0 (note figure 2) decreases output displacement but increases output force. For a constant piezoelectric element length a, increasing the width b has a negligible effect on displacement but increases output force. Decreasing the flexure thickness t increases displacement but decreases force. Finally, increasing t_f and w increases force and has a small effect on displacement.

One can see that there is considerable flexibility within the actuator design space to achieve a wide range of application-driven requirements. These requirements would likely be related to device size, weight, and force/displacement characteristics. Other considerations could include electromechanical efficiency, lifetime (not modeled here, but empirical results are described in section 7), and cost. In prior work [28], we optimized the free displacement of a similar device. Here we conducted a more general design study with the goal of demonstrating that the actuator can be designed to achieve a wide range of force/displacement characteristics.

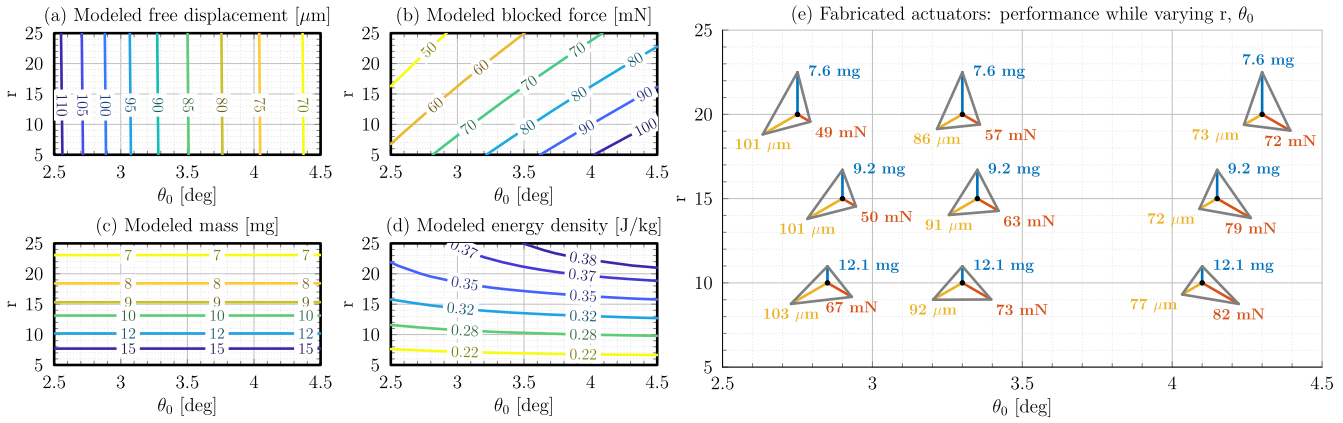

Figure 5. Design study results. The effect of varying the aspect ratio r and the nominal linkage angle θ_0 on modeled device performance is shown in plots (a–d). Measured performance, shown in plot (e), follows the trends predicted by the model and reasonably matches the predicted values. The data demonstrate that the actuator can be designed to achieve a wide range of performance characteristics. All data were taken at a 200 V_{pp} operating voltage.

Table 1. Variance-based sensitivity analysis. Each entry describes the effect of a design parameter or combination of parameters to the overall device performance (i.e., energy density). Sensitivity values were calculated via the Monte Carlo method with N = 2000 sample points.

	θ_0	r	t	w
θ_0	.21	.01	0	0
r		.67	0	.01
t			.04	0
w				.07

We also wanted to show that mechanical energy density, which captures information about device weight and its force/displacement characteristics, stays relatively constant across designs. Assuming an actuator has a linear force/displacement profile (i.e. constant output stiffness), its energy density is given by:

$$D_u = \frac{f_{block}\,\Delta y_{free}}{2m} \tag{13}$$

where f_{block}, Δy_{free}, and m are the blocked force, free displacement, and mass, respectively.

To determine which design parameters most affect energy density (and by extension, force and displacement), we performed a sensitivity analysis, the results of which are shown in table 1. We limited our analysis to the four parameters that can be easily varied during manufacturing: the nominal linkage angle θ_0, the aspect ratio $r = (a + 2c)/b$, the flexure thickness t, and the arm width w. Some parameters, such as the thickness of the piezoceramic t_p, are not easy to vary because they are contingent upon material availability. Moreover, some paraemeters, such as the length of the piezoceramic a are assumed to be governed by application requirements. Here, we used $a = 8$ mm for all designs. The sensitivity analysis was conducted by sampling $N = 2000$ random designs within the following ranges: $\theta_0 \in [1, 5°]$, $r \in [5, 25]$, $t \in [10, 50\ \mu\text{m}]$, and $w \in [100, 500\ \mu\text{m}]$. These were chosen to capture all possible designs that could be manufactured while excluding designs that would result in undesirably low output displacement or force.

From the sensitivity analysis, we determined that θ_0 and r were the most critical parameters in the design space. To validate our model and demonstrate that this type of actuator can be designed to achieve a wide range of performance goals, we fabricated nine actuators, varying θ_0 and r each in three ways.

5. Results

The performance of the fabricated actuators was found to reasonably match that predicted by the lumped parameter model, as shown in figure 5. Across all nine actuators, the mean relative error in predicted versus measured free displacement and blocked force were $6.5 \pm 0.7\%$ and $8.3 \pm 2.8\%$, respectively. We see that the model correctly predicts the trends in the data: as θ_0 increases, free displacement decreases and blocked force increases, and as r increases, free displacement decreases and blocked force decreases.

The voltage response of one of the best performing actuators ($r = 20$ and $\theta_0 = 3.3°$), is shown in figure 6. Both the lumped parameter model and the FEA accurately capture the measured free displacement of the actuator, though only the FEA well captures the measured blocked force. This is likely due to the simplifications made to the geometry in the lumped parameter model.

The free displacement voltage response measurements were taken with the actuator in a quasi-static state (1 Hz driving frequency) with a laser Doppler vibrometer (Polytec PSV-500). Voltage measurements were taken in increments of 20 V from 0 to 300 V_{pp}. For each applied voltage, the velocity during forty periods of the drive signal was measured, averaged over a single period, integrated to yield

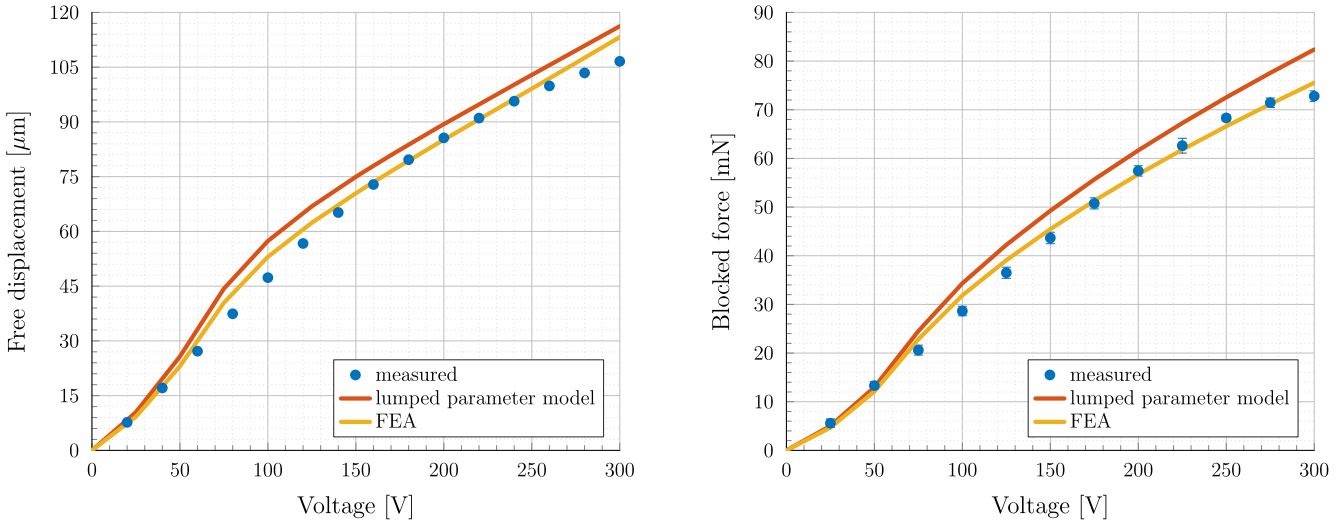

Figure 6. Modeled and measured free displacement and force for the high performing design: $r = 20$ and $\theta_0 = 3.3$ deg. Both the lumped parameter model and the FEA capture the measured free displacement data well (10.6% and 4.6% average relative error, respectively). The FEA captures the blocked force data well (5.7% error), and the lumped parameter model shows minor error (11.0%). The modeled values shown correspond to $Y_{cf} = 100$ GPa and the models are otherwise not fitted.

displacement, and recorded. The number of time averages was chosen to minimize the measurement error while maintaining a reasonable bound on total experiment time. Measurement error, defined as the average relative standard deviation, was found to be acceptably low (0.4%).

Actuator blocked force was measured under the same drive signal with a high resolution force sensor (ATI Nano 17). The actuators were mounted in turn on a linear stage to allow for precise alignment with the force sensor. They were positioned such that their linkages were undeformed at zero applied voltage and were kept in this position for all tests. The measurement error for the blocked force measurements was reasonably low (3.9%).

The transient response to sine, ramp, and step inputs is shown in figure 7. All measurements were taken using the laser Doppler vibrometer on an actuator ($r = 15$ and $\theta_0 = 3.3°$) that was slightly worse performing than the corresponding one used in the design study. In figure 7(a), we show the repeatability of the actuator in response to a 200 V_{pp} sine wave. The standard deviation of the response from the cyclic average, $\sigma = 55$ nm, is within the measurement noise of $\sigma = 144$ nm (recorded with no voltage input to the actuator). Thus, we concluded that the repeatability is bounded by the measurement noise. In the figure 7(b), an actuator resolution of 300 nm is demonstrated. Ramp threshold voltages of 200, 200.5, and 201 V were applied and actuator velocity was averaged over 100 cycles for each ramp voltage. The measurement noise for a null input with this averaging was $\sigma = 14$ nm. In figure 7(c), the transient response to a 100 V_{pp} step input is shown. Two resonances are visible, as can also be seen in the frequency response shown in figure 7(d). The lower resonance corresponds to the bulk motion of the piezoceramic, while the higher resonance corresponds to the oscillation of the output links.

6. Manufacturing

The actuators are straightforward to manufacture using a PC-MEMS manufacturing process, which in this case incorporated laser micromachining, plasma etching, chemical vapor deposition, and precision pin-aligned heat/pressure lamination. The process is explained in detail as follows:

(1) We began by laminating four sheets of unidirectional prepreg carbon fiber with thin polyimide sheets on top and bottom for electrical insulation. We used 30 μm thick high-modulus carbon fiber (QA-112, Taho Tanex) and 5 μm thick polyimide film (Kapton 30 EN, DuPont) such that the resulting laminate had a compressed thickness of 130 $\pm$ 2 μm. A programmable heat press was used for the lamination (Carver Auto Series NE). The resulting laminate became the bulk material from which the flextensional frame was machined.

(2) Next, we formed individual layers of carbon fiber/polymide, PZT-5H, and copper using laser micromachining. A 355-nm 8-W pulsed laser system was used (Oxford Lasers E Series). The laser spot size is power dependent and ranges from 7 to 20 μm, and the position accuracy ranges from 5 to 15 μm. Care was taken to minimize chemical composition change of the piezoceramic during laser processing, which occurs during melting and resolidification of the material and results in reduced dielectric strength, as described in [2]. In practice, this means using several thousand cut passes at a relatively low laser power (0.23 W at 20 kHz pulse rate) to limit melting of the piezoceramic. This is also the step in which we formed the flexures and linkage arms in the carbon fiber frame. We found that cutting these features at this step instead of cutting them after

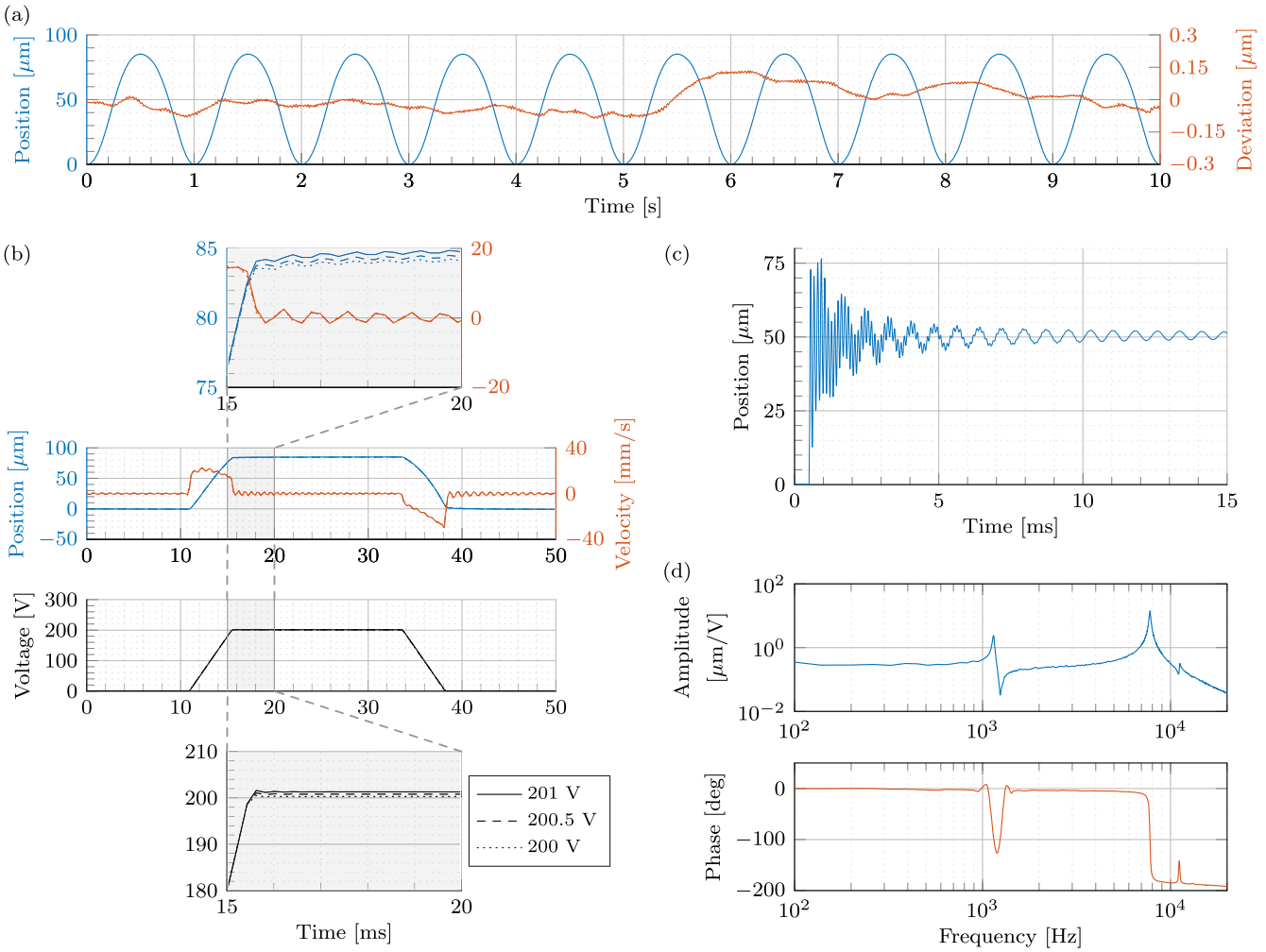

Figure 7. Actuator transient response in a variety of contexts: (a) Open loop repeatability while driven by a 200 V_{pp} sine wave. Absolute and deviatoric position are shown. Position deviation from cycle to cycle ($\sigma = 55$ nm) is within the measurement noise ($\sigma = 144$ nm). (b) Open loop position resolution. Position and velocity waveforms in response to ramp inputs are shown for ramp threshold voltages of 200, 200.5 and 201 V, and resolution of 300 nm is demonstrated. (c) Transient response to a 100 V_{pp} step input. Oscillations at both resonant frequencies seen in the frequency response (d) are visible.

lamination (steps 4-5) and reregistration (step 6) resulted in greater symmetry between the top and bottom portions of the frame. In principle, the spot size and repeatability of the laser system are small enough to control the flexure thickness to within a few μm, which would allow for precise matching of the flexure hinge thickness with a desired design value.

(3) After micromachinining individual layers, we ultrasonic cleaned (VWR 50HT) and plasma etched (Diener Electronic PCCE) the carbon fiber/polymide. A 2-min plasma etch in Argon was used. The purpose of these steps was to remove any residual carbon dust that was deposited during laser ablation and to prepare the surface for a parylene deposition. We deposited a 3 μm uniform coat of Parylene C in order to electrically isolate the carbon fiber/polymide frame from the rest of the actuator. Chemical vapor deposition was used for the parylene coating (Specialty Coating Systems PDS 2010).

(4) Next, we laser micromachined the prepreg carbon fiber that became the electrical and mechanical bridges between the carbon fiber/polymide/parylene frame and the piezoceramic. We then immediately (to avoid curing of the resin) placed the piezoceramic beams into slots in the frame and used alignment holes to mate the prepreg carbon fiber layers to the top and bottom of the frame. The structure was then partially cured (30 psi, 150 °C, 3 min) to transfer the carbon fiber from its paper backing onto to the frame. See figures 8(a)–(b) for detail. This is a key step that allows carbon fiber to be placed only where desired. It is important for three reasons: first, by minimizing the amount of carbon fiber used, unwanted resin flow onto the piezoceramic can be avoided; second, it is critical to avoid cutting carbon fiber during the release cut (step 6, below) because the ablation process releases carbon dust that binds to the substrate edges, shorting the device; third, because mismatches between

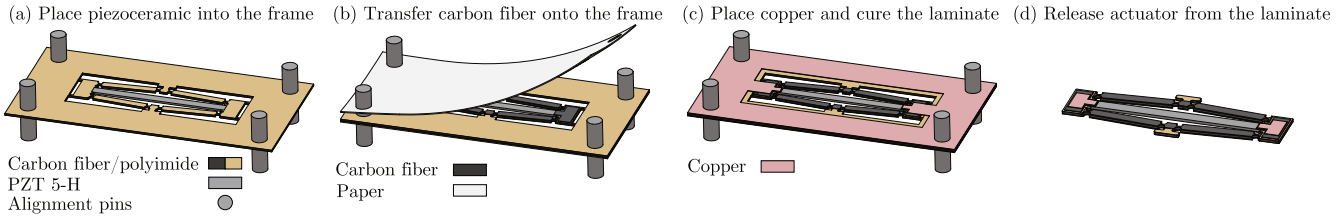

Figure 8. Key assembly steps: (a) Placement of piezoceramic beam in the laser-micromachined carbon fiber/polyimide frame. (b) Transfer of prepreg carbon fiber onto the assembly. (c) Placement of copper and curing of the laminate. (d) Release of the actuator from the laminate using laser ablation. A single actuator is shown for simplicity, but the process can be easily parallelized to enable batch fabrication.

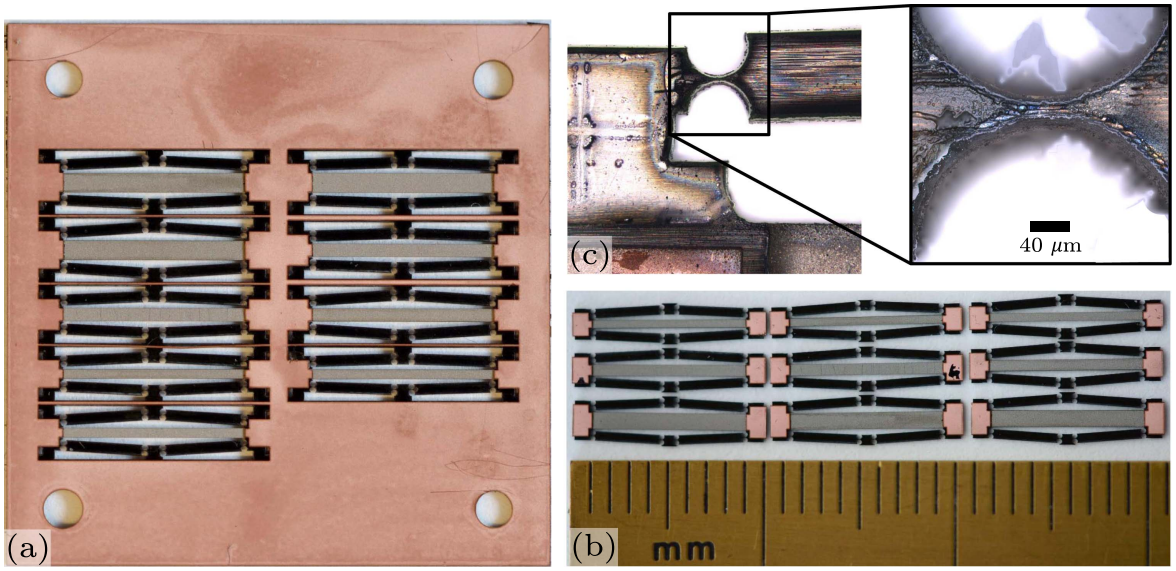

Figure 9. Batch fabricated actuators. (a) Laminated actuators before being released into individual pieces. (b) Actuators after being released from the substrate. These were the actuators manufactured for the design study. The aspect ratio r is varied in the vertical direction, and the nominal linkage angle is varied along the horizontal. (c) Zoomed-in image with a fabricated carbon fiber flexure.

the top and bottom layer of carbon fiber can cause warping in the laminate during curing, putting stress on the piezoceramic. Minimizing the amount of carbon fiber can minimize this effect. During the carbon fiber transfer process, compressible (Pacothane Technologies PACOPADS) and chemical resistant layers (FEP) were added to ensure a uniform pressure distribution and minimize resin flow, respectively.

(5) Following the carbon fiber transfer process, we peeled off the paper backing and mated the copper layers to the partially cured laminate (see figures 8(b)–(c)). The structure was then fully cured (30 psi, 150 °C max, 270 min), once again with the temporary addition of compressible and chemically resistant layers. A typical laminate is shown in figure 9(a).

(6) We then registered the laminate to the laser micromachining system using alignment fiducials and cut off the exterior tabs to release the device from the substrate. Once again, we were careful to avoid cutting through the carbon fiber frame in locations where electrical signals are present, so as to avoid shorting the device via conductive carbon dust.

(7) After the actuators were released from the substrate, they were cleaned with isopropyl alchohol to remove any carbon dust that was deposited during laser ablation. We typically placed the actuators in an 80 °C ultrasonic bath for 5 min. Removing the carbon dust minimizes the risk of shorting and is especially important for high-field operation. The set of released and cleaned actuators used in the design study are shown in figure 9(b), and a close-up view of a fabricated flexure hinge is shown in figure 9(c).

7. Discussion

Though we have herein explored many dimensions of actuator design and fabrication–lumped parameter and nonlinear finite element modeling, sensitivity analysis, and batch fabrication using an emerging manufacturing paradigm–many interesting questions remain. Primary among them is what types of devices this actuator might be useful in. One such device, a microgripper, is shown in figures 10(a)–(c). It was constructed through minor modification to one of the actuators used in the design study, and is able to grip objects of

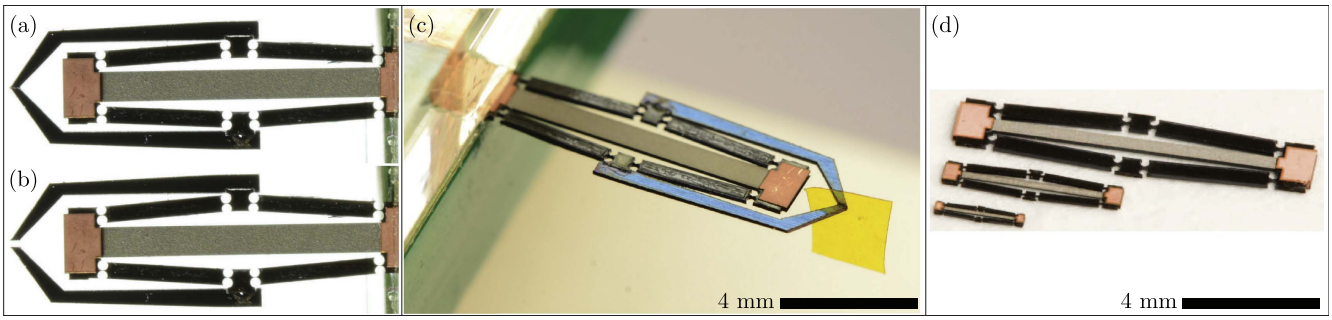

Figure 10. (a–c) Microgripper fabricated from a single flextensional actuator. The actuator is grounded at the base of the piezoceramic element, and the output links move away in equal and opposite directions from the center of the actuator when an external voltage is applied. (d) Half and quarter-sized actuators shown with full-size actuator for comparison. The half and quarter-sized actuators were fabricated with the same process that was used for the full-size actuator, though thinner piezoceramic and carbon fiber (60 μm) was used for the smaller devices.

thickness 10–100 μm. It uses the actuator in its two-output configuration: the base of the piezoceramic beam is mechanically grounded and the output links actuate bi-directionally. One intriguing possibility with this device is to leverage its high bandwidth in de-grasping: to vibrate the actuator in order to break the surface forces that develop between the gripper and a grasped object. Other potential applications lie in micro-optics, either in micro-focusing or micro-zoom modules, or in micro-laser systems, such as miniature galvanometer scanners in which mirrors steer a laser beam at ultra-high speeds.

Related to the question of applicability is that of scalability: how small can we make it, and does its performance change as we decrease size? We have begun investigating these questions, and we have successfully manufactured the half and quarter-sized actuators shown in figure 10(d). The most challenging dimension to properly scale is the thickness of the actuator, as carbon fiber is only available in discrete thicknesses, and piezoceramic cannot be easily ground down lower than 50 μm. We used 60 μm for both the half and quarter-sized actuators (also from Piezosystems, Inc). The 60 μm piezoceramic is much more fragile than the 135 μm, and thus requires exceptionally delicate handling. For the carbon fiber, we formed a laminate of two sheets of carbon fiber (instead of four) and sanded it down to 54 μm, allowing the parylene coat to add the last 6 μm of thickness to the frame. These actuators are still under development, though early results are promising.

Other key questions remain with respect to sensing and control. If the actuator were to be used in a closed-loop control system for one of the applications described above, sensors would need to be integrated, dynamics derived, and a control law implemented. For sensing, a current based method would likely be the most straightforward to implement. Closed-loop control is likely necessary for accurate position control due to the inherent hysteresis within the piezoceramic.

With regard to lifetime, we conducted a preliminary fatigue test and found that the actuator was able to complete 7 million cycles under free displacement without failure when driven by a 100 Hz sinusoidal signal at 100 V. Further tests are needed to characterize lifetime over a range of operating conditions.

The maximum achieved energy density of 0.51 Jkg^{-1} is a tenfold increase over the previously described version of this device in [28]. The key design improvements were the use of a higher modulus material for the frame, slightly increasing the nominal linkage angle, and increasing the aspect ratio of the piezoceramic element. These considerations are connected by the need to properly size the piezoceramic compressive stiffness to the compressive stiffness of the linkage arms and flexures. Another important design improvement was the incorporation of insulating materials (i.e., polyimide and parylene) to allow for higher voltage operation.

8. Conclusion

We have described a meso scale actuator formed from a piezoceramic element and a carbon fiber amplification frame. The carbon fiber frame has flexures formed in it to allow rotation in key locations. Together, the piezoceramic and the amplification frame produce output displacements on the order of 100 μm and blocked forces on the order of 70 mN. A design study was performed to show that our model accurately predicts trends in device performance and that force/displacement characteristics can be tailored for specific applications. A batch manufacturing process for the device was elucidated. Lastly, an actuator was integrated into a microgripper, and several other application areas for the actuator were described.

Acknowledgments

The authors thank Joshua Gafford and Kaushik Jayaram for many insightful discussions, and they gratefully acknowledge support from the Army Research Office (DURIP programs #W911NF-13-1-0311 and #W911NF-16-1-0282), the National Science Foundation under a Graduate Research Fellowship, and the Wyss Institute for Biologically Inspired Engineering at Harvard University. Any opinions, findings, and conclusions or recommendations expressed in this material are those of the authors and do not necessarily reflect the views of the Army

Research Office, the National Science Foundation, or the Wyss Institute.

ORCID iDs

Peter A York https://orcid.org/0000-0001-7411-5087

References

[1] Wood R J, Steltz E and Fearing R S 2005 Optimal energy density piezoelectric bending actuators *Sensors and Actuators A: Physical* **119** 476–88

[2] Jafferis N T, Smith M J and Wood R J 2015 Design and manufacturing rules for maximizing the performance of polycrystalline piezoelectric bending actuators *Smart Mater. Struct.* **24** 065023

[3] Yoon K-J, Park K-H, Lee S-K, Goo N-S and Park H-C 2004 Analytical design model for a piezo-composite unimorph actuator and its verification using lightweight piezo-composite curved actuators *Smart Mater. Struct.* **13** 459

[4] Jafferis N T, Lok M, Winey N, Wei G-Y and Wood R J 2016 Multilayer laminated piezoelectric bending actuators: design and manufacturing for optimum power density and efficiency *Smart Mater. Struct.* **25** 055033

[5] DeVoe D L and Pisano A P 1997 Modeling and optimal design of piezoelectric cantilever microactuators *J. Microelectromech. Syst.* **6** 266–70

[6] Oldham K R, Pulskamp J S, Polcawich R G and Dubey M 2008 Thin-film PZT lateral actuators with extended stroke *J. Microelectromech. Syst.* **17** 890–9

[7] Dogan A, Xu Q, Onitsuka K, Yoshikawa S, Uchino K and Newnham R E 1994 High displacement ceramic metal composite actuators (moonies). *Ferroelectrics* **156** 1–6

[8] Dogan A, Uchino K and Newnham R E 1997 Composite piezoelectric transducer with truncated conical endcaps 'cymbal' *IEEE Transactions on Ultrasonics, Ferroelectrics, and Frequency Control* **44** 597–605

[9] Poikselkä K L, Leinonen M, Palosaari J, Vallivaara I, Röning J and Juuti J 2017 Novel genetically optimised high-displacement piezoelectric actuator with efficient use of active material *Smart Mater. Struct.* **26** 095022

[10] Conway N J, Traina Z J and Kim S-G 2007 A strain amplifying piezoelectric MEMS actuator *J. Micromech. Microeng.* **17** 781

[11] Seo Y H, Choi D-S, Lee J-H, Je T-J and Whang K-H 2006 Laterally driven thin film PZT actuator with high-aspect-ratio silicon beam for stroke amplification *Sensors and Actuators A: Physical* **127** 302–9

[12] Cedrat Technologies. Apa30uxs. http://cedrat-technologies.com/fileadmin/user_upload/cedrat_groupe/Mechatronic_products/Piezo_actuators_electronics/APAs/Technical_Datasheet/APA30XS_GB_v4.0.pdf, November 2014.

[13] Neal D M and Harry Asada H 2014 Bipolar piezoelectric buckling actuators *IEEE/ASME Transactions on Mechatronics* **19** 9–19

[14] Torres J and Harry Asada H 2014 High-gain, high transmissibility PZT displacement amplification using a rolling-contact buckling mechanism and preload compensation springs *IEEE Transactions on Robotics* **30** 781–91

[15] Ueda J, Secord T W and Harry Asada H 2010 Large effective-strain piezoelectric actuators using nested cellular architecture with exponential strain amplification mechanisms *IEEE/ASME Transactions on Mechatronics* **15** 770–82

[16] Kim J H, Kim S H and Kwak Y K 2004 Development and optimization of 3-d bridge-type hinge mechanisms *Sensors and Actuators A: Physical* **116** 530–8

[17] Hemsel T and Wallaschek J 2000 Survey of the present state of the art of piezoelectric linear motors *Ultrasonics* **38** 37–40

[18] Uchino K 1998 Piezoelectric ultrasonic motors: overview *Smart Mater. Struct.* **7** 273

[19] Morita T 2003 Miniature piezoelectric motors *Sensors and Actuators A: Physical* **103** 291–300

[20] Park J, Keller S, Carman G P and Hahn H T 2001 Development of a compact displacement accumulation actuator device for both large force and large displacement *Sensors and Actuators A: Physical* **90** 191–202

[21] Yoshida R, Okamoto Y and Okada H 2002 Development of smooth impact drive mechanism (2nd report)-optimization of waveform of driving voltage *Int. J. Jpn. Soc. Precis. Eng.* **68** 536–41

[22] Henderson D A 2006 Simple ceramic motor... inspiring smaller products *International Conference on New Actuators* **50** 10

[23] Mohammadi F, Kholkin A L, Jadidian B and Safari A 1999 High-displacement spiral piezoelectric actuators *Appl. Phys. Lett.* **75** 2488–90

[24] Robbins W P, Polla D L, Tamagawa T, Glumac D E and Tjhen W 1991 Design of linear-motion microactuators using piezoelectric thin films *J. Micromech. Microeng.* **1** 247

[25] Budd K D, Dey S K and Payne D A 1985 Sol-gel processing of $PbTiO_3$, $PbZrO_3$, PZT, and PLZT thin films *Br. Ceram. Proc.* **36** 107–21

[26] Muralt P 2000 Ferroelectric thin films for micro-sensors and actuators: a review *J. Micromech. Microeng.* **10** 136

[27] Whitney J P, Sreetharan P S, Ma K Y and Wood R J 2011 Pop-up book mems *J. Micromech. Microeng.* **21** 115021

[28] York P A and Wood R J 2017 A geometrically-amplified in-plane piezoelectric actuator for mesoscale robotic systems *IEEE International Conference on Robotics and Automation* pp 1263–8